Templating Three-Dimensional Self-Assembled Structures in Bilayer Block Copolymer Films

A. Tavakkoli K. G.,[1,2] K. W. Gotrik,[3] A. F. Hannon,[3] A. Alexander-Katz,[3]
C. A. Ross,[3]* K. K. Berggren[1]*

The registration and alignment of a monolayer of microdomains in a self-assembled block copolymer thin film can be controlled by chemical or physical templating methods. Although planar patterns are useful for nanoscale device fabrication, three-dimensional multilevel structures are required for some applications. We found that a bilayer film of a cylindrical-morphology block copolymer, templated by an array of posts functionalized with a brush attractive to the majority block, can form a rich variety of three-dimensional structures consisting of cylinder arrays with controllable angles, bends, and junctions whose geometry is controlled by the template periodicity and arrangement. This technique allows control of microdomain patterns and the ability to route and connect microdomains in specific directions.

Complex nanoscale pattern formation on two-dimensional (2D) surfaces can be achieved using template-assisted self-assembly of block copolymer (BCP) thin films. Approaches that depend on sparse patterns of lithographically defined chemical templates (*1*–*4*) or physical templates (*5*–*10*) have focused on controlling a single layer of BCP microdomains. This layer is then used as a mask, in combination with conventional planar processing techniques such as liftoff and etching, to fabricate devices including patterned magnetic recording media, nanowire transistors, flash memory, and gas sensors (*11*–*16*).

The inherent 3D nature of self-assembled BCPs suggests their possible use in fabricating 3D devices such as cross-point structures in a single step, rather than building up the structure sequentially. There have been reports of the fabrication of 3D structures by self-assembly of thicker BCP films or by sequential stacking and cross-linking of BCP films (*17*–*25*), but stacking methods have disadvantages for the fabrication of 3D structures because of the difficulty of aligning multiple layers, the large number of processing steps required, and the poor order of the resulting patterns. In the absence of templating, the achievable geometries of bilayer BCPs are limited; for example, in a bilayer cylindrical-morphology BCP thin film, the cylinders in each layer share the same orientation, whereas in a spherical-morphology BCP the spheres form two offset close-packed layers (*26*).

Chemical templating of bilayers of spherical microdomains (*17*–*19*) and lamellae (*20*) has been shown to yield square symmetry patterns and coupled perforated lamellae, respectively. A wider range of 3D BCP structures can be achieved by confinement of the BCP within parallel surfaces, narrow pores, or spherical cavities, which produce structures such as helices, cylindrical shells, and stacked disks or tori not found in bulk (*24*, *25*, *27*). However, these processes do not enable the formation of interconnected structures in which the microdomains can be routed or connected arbitrarily over a large area.

Here, we show by experiment and self-consistent field theory that simple periodic arrays of posts can give control over the orientation of each layer of cylinders in a bilayer BCP film, enabling the orientation of each of the two layers of cylinders to be controlled independently, simultaneously, and locally. This was accomplished by functionalizing the posts with a majority-block homopolymer brush, which rendered the posts attractive to the majority-block matrix and repulsive to the minority-block cylindrical microdomains. The resulting self-assembled structures are understood by considering the commensurability between the post period and the equilibrium BCP period, as well as the energy costs associated with in-phase stacking of alternate layers of cylindrical microdomains. Connections between cylinders in different layers can form a cross-point–like architecture, and by locally controlling the post periodicity and arrangement, one can create specific defects, bends, and junctions in the top and bottom layers independently. Moreover, noncylindrical structures such as perforated lamellae, as well as periodic superstructures with double the period of the template, can be created. These results provide an approach for making 3D structures useful in applications (e.g., cross-point memory devices) that require the precise placement of nanowires in three dimensions. As an additional advantage, this process can produce rectangular or square-symmetric structures, which are useful in applications such as fabricating integrated circuit interconnects or bit-patterned media (*28*).

Figure 1A shows a diagram of the major steps of the 3D templating process. In the first step, hydrogen silsequioxane (HSQ) was spin-coated at 40 ± 2 nm thickness on Si (100) substrates. The post array templates were fabricated by means of electron-beam lithography of the HSQ resist at an acceleration voltage of 30 kV, beam current of 300 pA, and dot doses of 40 to 116 fC. After development and HSQ hardening by use of an oxygen plasma asher, the final post height was 33 ± 2 nm. Next, the substrates and posts were chemically functionalized with hydroxyl-terminated polystyrene (1 kg mol^{-1}, 2 nm thick), which corresponds to the majority block of the BCP. A cylindrical-morphology poly(styrene-b-dimethylsiloxane) (PS-b-PDMS) BCP (45.5 kg mol^{-1}, fraction of PDMS = 32%) was spin-coated onto the substrates with the post templates to a thickness of 42 ± 1 nm. Solvent vapor annealing of the BCP thin film was done using a 5:1 volume ratio mixture of toluene and heptane, which resulted in swelling the BCP film to 101 ± 3 nm (~$3L_0$) and resulted in the formation of a bilayer of in-plane PDMS cylinders in a PS matrix with in-plane periodicity (L_0) of ~36 nm. After the solvent vapor anneal, a rapid quench was done within 1 s, which was believed to freeze in the annealed morphology as the solvent vapor leaves the film (*29*). Lastly, an oxygen reactive-ion etch was used to remove the PS block, further reducing the film thickness and revealing the oxidized PDMS (ox-PDMS) patterns (*30*).

Both layers of cylinders are clearly visible in scanning electron micrographs (SEMs) after etching (Fig. 1, B and C) and are oriented with respect to the lattice vectors of the post lattice. The PDMS cylinders typically lie between the PS-coated posts (Fig. 1A, step 4) because of the PS brush, unlike the case of PDMS-coated posts where the PDMS cylinders lie atop rows of posts (*31*). To describe the resulting morphologies systematically, we introduce a notation [(*a b*),(*c d*)] in which (*a b*) refers to the top layer and (*c d*) refers to the bottom layer of cylinders; (*a b*) and (*c d*) are analogous to the 2D Miller indexing of crystal lattice planes. For example, if $a = 2$, then for the top layer the spacing between cylinders in the *x* direction is half the spacing between the posts (here, the *y* direction is that with the smaller periodicity). In cases where the cylinders lie on top of the posts, a prime [e.g., $(a\ b)'$] is included in the notation. Some post lattices generate noncylinder morphologies, which are designated S, E, or B for spheres, ellipsoids, or square-symmetry perforated lamellae, respectively, in place of the Miller indices.

Figure 1B shows a bilayer film templated by a rectangular array of PS-functionalized posts 21 nm in diameter and 33 nm in height, with *x* direction periodicity of 100 nm and *y* direction periodicity of 36 nm. Figure 1C shows magnified and cross-sectional SEMs of regions inside and outside the templated region. Outside the templated region, the top and bottom layers of ox-PDMS cylinders shared local orientation,

---

[1] Department of Electrical Engineering and Computer Science, Massachusetts Institute of Technology, Cambridge, MA 02139, USA. [2] NUS Graduate School for Integrative Sciences & Engineering (NGS), Singapore 117456, Singapore. [3] Department of Materials Science and Engineering, Massachusetts Institute of Technology, Cambridge, MA 02139, USA.

*To whom correspondence should be addressed. E-mail: caross@mit.edu (C.A.R.); berggren@mit.edu (K.K.B.)

with the cylinders in the top layer lying in between those of the bottom layer without showing long-range order. Inside the templated region, the cylinders in the top and bottom layers did not generally share local orientation between the posts because of the energetic cost associated with incommensurability. As a result, the top cylinders instead self-assembled into a meshlike array that covered the entire templated region (see fig. S1 for an example in which the cylinders formed a different angle between the two layers, and fig. S2 for a cross-sectional image from a different viewing angle). Figure 1, D and E, shows another example of templated bilayer films in which additional columns of square or parallelogram-shaped holes were generated between the posts. These results demonstrate the ability to control the orientation of the individual layers of microdomains within a bilayer.

By changing the post periodicities in the *x* and *y* directions, we achieved a wide range of orientations and morphologies of both the top and bottom layers of microdomains. Figure 2 shows examples, including parallel top and bottom PDMS cylinders (Fig. 2, A and B); meshlike structures (Fig. 2, C to F); structures containing a layer of ellipsoids, spheres, or square perforated lamellae (Fig. 2, G to I); and periodic superstructures (Fig. 2, J and K). Each of these 3D structures was observed within specific ranges of post periodicities in the *x* and *y* directions, and the cylinders were oriented perpendicular to the direction in which the post periodicity was commensurate with the BCP period. In general, the top layer of cylinders formed the more commensurate arrangement. These structures are consistent with the equilibrium morphologies observed in the self-consistent field theory (SCFT) simulations, which modeled the morphologies present when the film was fully swollen (before quenching).

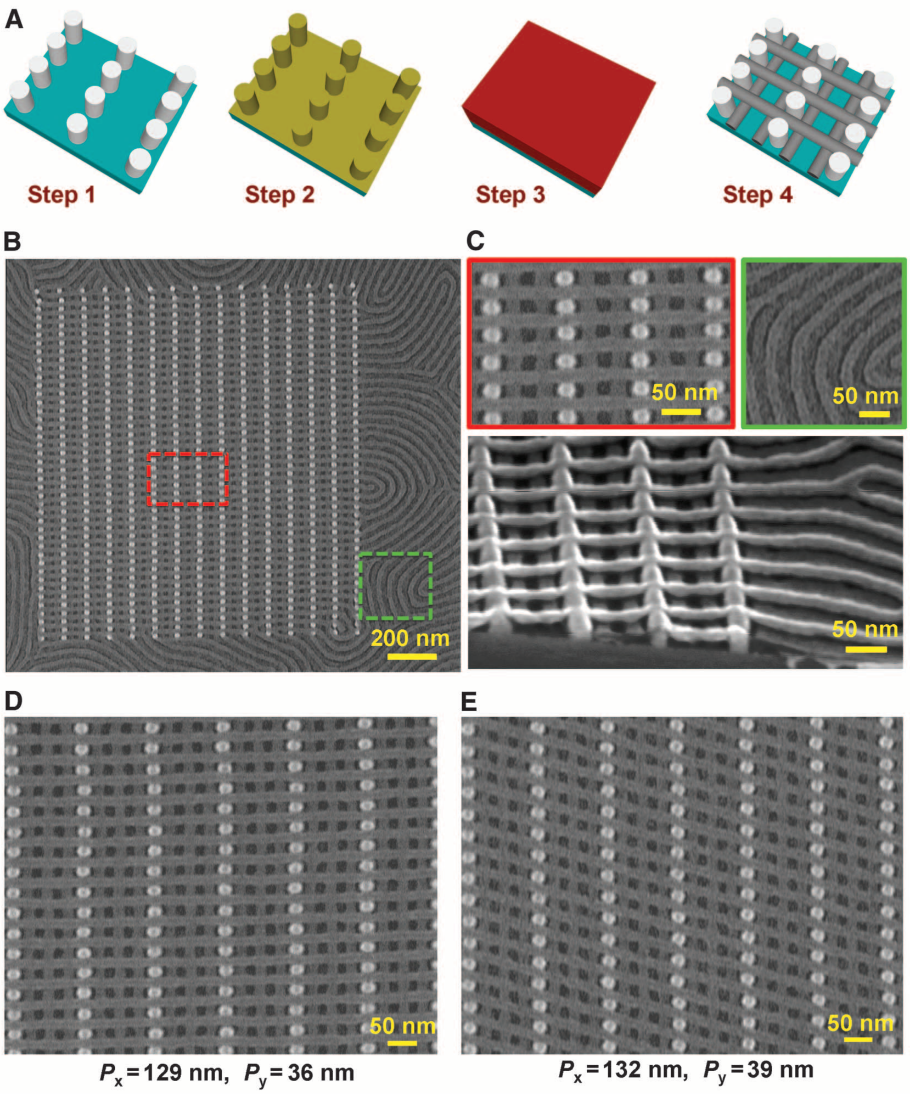

$P_x = 129$ nm, $P_y = 36$ nm $P_x = 132$ nm, $P_y = 39$ nm

Fig. 1. Fabrication of 3D structures. (**A**) The major steps of the fabrication process for the 3D structures: step 1, fabricating the post templates by electron-beam lithography; step 2, chemically functionalizing posts with a PS brush; step 3, spin coating and solvent annealing of the BCP; step 4, removing the PS matrix by an oxygen reactive-ion etch and leaving the ox-PDMS patterns on the substrate. (**B**) SEM of an etched [(0 1),(2 0)] bilayer structure on a substrate. (**C**) Upper magnified SEMs (red and green borders refer to Fig. 1B) and lower cross-sectional (lower inset) SEM of the regions inside and outside the template. (**D** and **E**) SEMs of a [(0 1),(3 0)] perpendicular structure (D) and a [(1 1),(3 0)] angled mesh-shaped structure (E) formed from two layers of ox-PDMS cylinder arrays. The bright dots and the light gray linear features represent HSQ and ox-PDMS, respectively.

Figure 2, A and B, shows cases where the cylinders in both layers were oriented parallel (in the *y* direction, Fig. 2A; in the diagonal direction, Fig. 2B) and the cylinders in the top layer were offset from those of the bottom layer, as seen in the untemplated bilayer film. The offset stabilizes the parallel arrangement, but it incurs an energy penalty if there is contact between the cylinders and posts. The top layer of cylinders could overlay the posts (Fig. 2B), but in cases where the bottom layer lay along a line of posts, it was interrupted to form dash shapes (fig. S3).

In Fig. 2, C to F, the cylinders in the two layers became oriented in two different directions and made a mesh-shaped structure. Mesh-shaped structures occurred when the post period in the *y* or diagonal direction was equal to the BCP period, favoring alignment of one layer of cylinders perpendicular to the *y* or diagonal direction, but the period in the *x* direction was slightly less than an integer multiple of the BCP period. In this case, the parallel alignment seen in Fig. 2, A and B, is less favorable than a mesh structure. Depending on the commensurability of the post lattice, the angle of the mesh was 90° (Fig. 2, C and E) or more (Fig. 2, D and F).

The mesh structures of Fig. 2, C to F, can be generalized to include larger numbers of cylinders subdividing the *x*-axis period, as shown in Fig. 1, D and E, where the post periods in the *x* direction were less than 4 times the BCP period. The dimensions of the square and parallelogram holes in all the mesh-shaped patterns were 18 by 18 nm, and their periods in the *y* direction were ~36 nm, matching the BCP period. The resulting parallelogram and square holes demonstrated sharp corners relative to those fabricated using conventional lithography, which suggests a role for such structures in the generation of nanoscale square or rhombic features or pits.

Figure 2, G to I, shows examples in which the bottom layer of microdomains formed ellipsoids (Fig. 2G) or spheres (Fig. 2H) between the posts, and square perforated lamellae in which the holes in the PDMS surrounded the posts (Fig. 2I). These structures occurred when the BCP period was not commensurate with either the *x* or *y* direction spacing. We also observed periodic superstructures in which the structure alternated between two morphologies between adjacent columns of posts, resulting in twice the period of the post lattice. Examples are shown in Fig. 2, J and K.

To analyze the experimental morphologies, we constructed a phase diagram (Fig. 2L) in

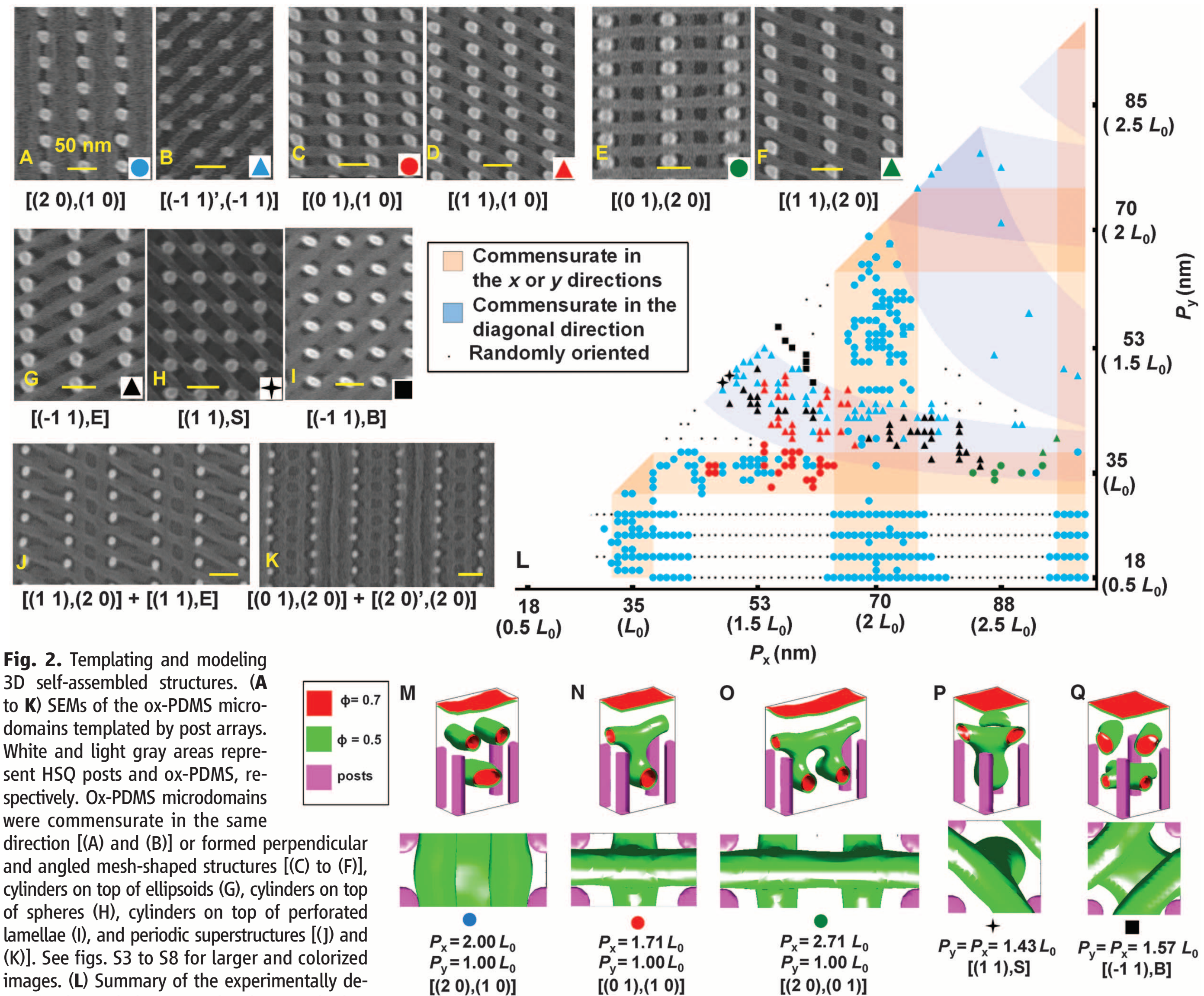

Fig. 2. Templating and modeling 3D self-assembled structures. (**A** to **K**) SEMs of the ox-PDMS microdomains templated by post arrays. White and light gray areas represent HSQ posts and ox-PDMS, respectively. Ox-PDMS microdomains were commensurate in the same direction [(A) and (B)] or formed perpendicular and angled mesh-shaped structures [(C) to (F)], cylinders on top of ellipsoids (G), cylinders on top of spheres (H), cylinders on top of perforated lamellae (I), and periodic superstructures [(J) and (K)]. See figs. S3 to S8 for larger and colorized images. (**L**) Summary of the experimentally determined morphologies. Circles denote cylinders oriented along *x* or *y*; triangles, stars, and squares denote cylinders oriented in a diagonal direction. (**M** to **Q**) SCFT simulation results for representative post periods. Top images, isometric views; bottom images, top-down views. Surface contours of constant minority-block (PDMS) density ϕ are plotted; ϕ = 0.5 represents the boundary between the PS and PDMS blocks.

which the various morphologies are plotted as a function of post period P_x and P_y in the *x* and *y* directions, respectively. The periods are expressed as multiples of L_0, the equilibrium period of cylinders in an untemplated film annealed under the same conditions. Superposed on this graph are vertical and horizontal colored bands representing approximate commensurate conditions (i.e., when P_x and P_y are within ±9% of an integer multiple of L_0). Curved colored bands represent commensurate conditions for the diagonal spacing, for example, $(P_x^2 + P_y^2)^{1/2}$. A value of 9% was chosen because BCP films have been found to adjust their period in response to a template by up to approximately this amount (*31*, *32*).

Examination of Fig. 2L shows that the observed morphologies correspond well with the commensurate template conditions. The correspondence indicates that commensurability in both *x* and *y* directions plays a dominant role in determining which morphology forms.

SCFT simulations were carried out to investigate the 3D structure of the features, as well as the metastability of the structures observed. The thickness of the unit cell was set to the swelled BCP thickness observed during the solvent annealing, which was ~3.00L_0; the post diameter and height were 0.71L_0 and 1.64L_0, respectively (see supplementary text). The simulation results showed the same general trends as the experiments. Parallel cylinders were predicted by the SCFT simulation for *x* direction post periods equal to integer multiples of L_0 (Fig. 2M). Perpendicular mesh-shaped structures were predicted for *x* direction periods less than an integer multiple of L_0 (2L_0, 3L_0) and *y* direction periods equal to L_0, as was seen in the experiments (Fig. 2, N and O). Different morphologies in the two layers were predicted by SCFT, such as cylinders over spheres (Fig. 2P) and cylinders over perforated lamellae (Fig. 2Q). However, simulations of two unit cells did not predict the observed superstructures. Consideration of factors not included in the SCFT, such as bending of the posts or non-equilibrium formation during the solvent vapor annealing, may be required to explain these structures. Recently, crossed cylinders were also predicted in a BCP confined between parallel surfaces with highly incommensurate spacing (*27*).

In the simulations, the cylinders in the two layers were often connected (Fig. 2, N to P). These connections between the two layers may be

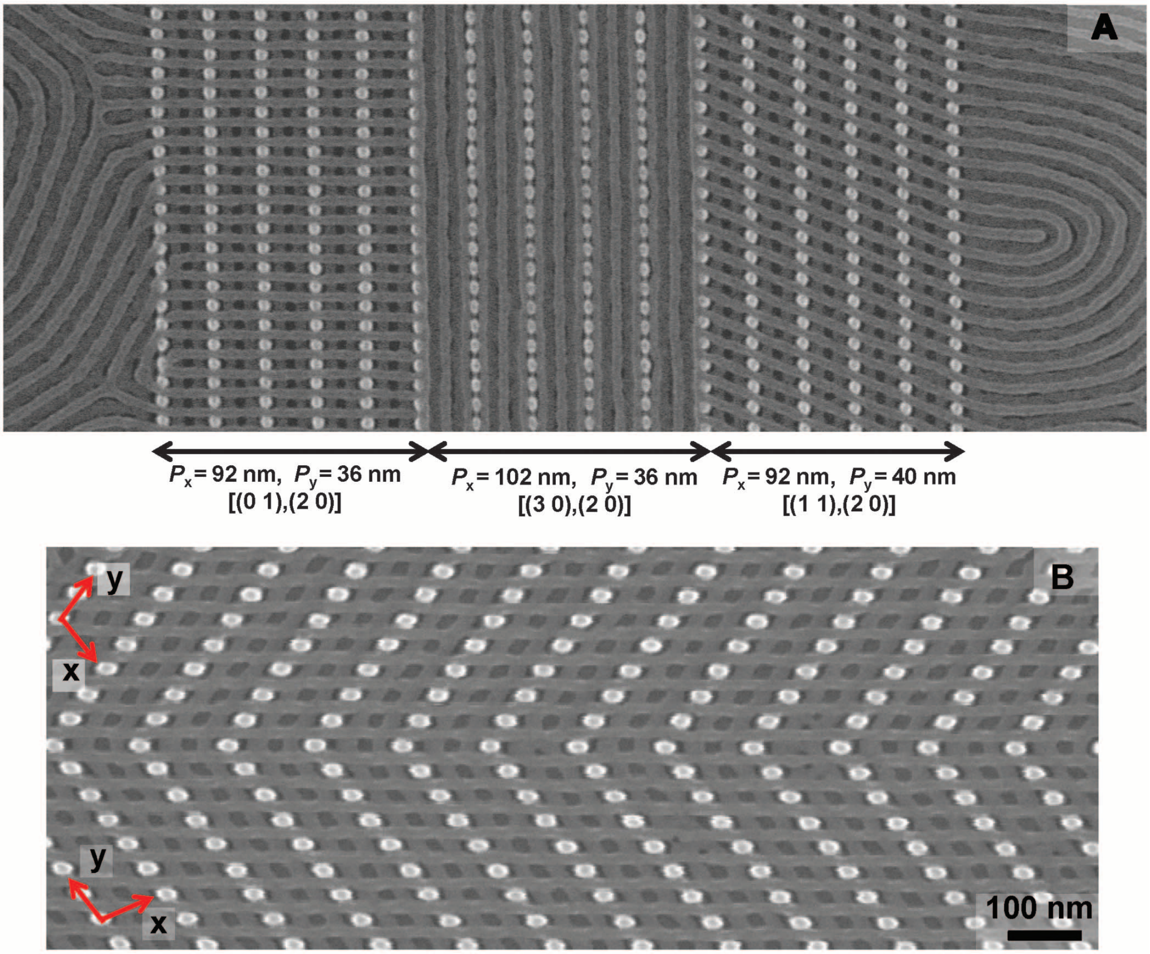

Fig. 3. Templated 3D bends and junctions. (**A**) SEM of a locally controlled structure fabricated by changing the post periodicity in the *x* and *y* directions. From left to right, the structures changed from [(0 1),(2 0)] to [(3 0),(2 0)] and then to [(1 1),(2 0)]. (**B**) SEM of a locally controlled structure fabricated by changing the post lattice orientation. Top to bottom, the [(–1 1),(2 0)] structure contained a mirror plane parallel to the [1 –1] direction of the lower post lattice. The *x* and *y* axes make an angle of 107°. White and light gray areas represent HSQ and ox-PDMS, respectively.

metastable defects. However, there is also experimental evidence in the mesh-shaped structures for these connections (fig. S9). By seeding the simulation with a field configuration that represented a mesh-shaped structure without a connection, we found that the energies of the connected versus unconnected systems were too close to distinguish a lower-energy state (see supplementary text). Thus, local connections between cylinders are likely to be present in the system and should be considered in postprocessing applications for these patterns.

In addition to controlling the alignment and morphology of the PDMS microdomains in two different layers, we were also able to locally control the alignment of the microdomains to form more complicated patterns with specific defects, bends, and neighboring junctions. In particular, junctions and bends were placed in either of the layers of cylindrical microdomains. Two approaches were used, separately or in combination, to fabricate such aperiodic structures: (i) a post array with a variation in the post periodicity in one or both directions to fabricate bends and junctions (T and angled junctions) in the top layer; and (ii) a post lattice whose orientation varied while the period was constant to fabricate bends and junctions (T, angled, and Y junctions) in the bottom layer. These types of bends and junctions could potentially be used to fabricate integrated-circuit elements (*33*). Figure 3A shows a structure made by the first approach in which, by increasing the post periodicity in the *x* direction, a [(0 1),(2 0)] structure joined with a [(3 0),(2 0)] structure and, by increasing the post periodicity in the *y* direction and decreasing it in the *x* direction, the [(3 0),(2 0)] structure joined with a [(1 1),(2 0)] structure. Thus, the bottom layer of cylinders had a fixed direction (*y* direction) and only the direction of the top cylinders was varied; structures such as T junctions formed where the different orientations met. Figure 3B shows a structure made using the second approach in which, by changing the post arrangement, the [(–1 1),(2 0)] structure contained a mirror plane parallel to the [1 –1] direction of the lower post lattice. The top layer of cylinders had a fixed direction (*x* direction), and only the direction of the bottom cylinders was varied. Figure S14 shows an example of a Y junction in which two cylinders merged into one cylinder, and figs. S15 to S17 show additional images of similarly fabricated structures.

The central result of this work is the independent and simultaneous control of the morphology and orientation of two layers of BCP microdomains guided by an array of functionalized posts. This forms the basis for the creation of more complicated structures such as cylinders with specific defects, bends, and junctions, as well as noncylindrical morphologies, and connections between the top and bottom layers of cylinders can be made (fig. S18). The strategies demonstrated here for the 3D routing of dense nanoscale cylindrical features using a single self-assembly step could facilitate new methods for nanoscale device manufacturing when combined, for example, with processes that convert microdomains selectively into functional materials such as oxides or metals (*34*).

References and Notes

1. R. Ruiz *et al.*, *Science* **321**, 936 (2008).
2. J. Y. Cheng, C. T. Rettner, D. P. Sanders, H. Kim, W. D. Hinsberg, *Adv. Mater.* **20**, 3155 (2008).
3. S. O. Kim *et al.*, *Nature* **424**, 411 (2003).
4. L. Rockford *et al.*, *Phys. Rev. Lett.* **82**, 2602 (1999).
5. I. Bita *et al.*, *Science* **321**, 939 (2008).
6. S. Park *et al.*, *Science* **323**, 1030 (2009).
7. R. A. Segalman, H. Yokoyama, E. J. Kramer, *Adv. Mater.* **13**, 1152 (2001).
8. J. Y. Cheng, C. Ross, E. L. Thomas, H. I. Smith, G. J. Vancso, *Adv. Mater.* **15**, 1599 (2003).
9. C. T. Black, O. Bezencenet, *IEEE Trans. Nanotechnol.* **3**, 412 (2004).
10. R. Ruiz, R. L. Sandstrom, C. T. Black, *Adv. Mater.* **19**, 587 (2007).
11. D. J. Milliron, S. Raoux, R. M. Shelby, J. Jordan-Sweet, *Nat. Mater.* **6**, 352 (2007).
12. J. Y. Cheng, W. Jung, C. A. Ross, *Phys. Rev. B* **70**, 064417 (2004).

13. C. T. Black, *Appl. Phys. Lett.* **87**, 163116 (2005).
14. T. Thurn-Albrecht *et al.*, *Science* **290**, 2126 (2000).
15. K. Naito, H. Hieda, M. Sakurai, Y. Kamata, K. Asakawa, *IEEE Trans. Magn.* **38**, 1949 (2002).
16. Y. S. Jung, W. Jung, H. L. Tuller, C. A. Ross, *Nano Lett.* **8**, 3776 (2008).
17. S. Ji *et al.*, *Adv. Mater.* **23**, 3692 (2011).
18. S.-M. Park, G. S. W. Craig, Y.-H. La, P. F. Nealey, *Macromolecules* **41**, 9124 (2008).
19. S. M. Park, G. S. W. Craig, Y.-H. La, H. H. Solak, P. F. Nealey, *Macromolecules* **40**, 5084 (2007).
20. K. Ch. Daoulas *et al.*, *Phys. Rev. Lett.* **96**, 036104 (2006).
21. H. Jung *et al.*, *ACS Nano* **5**, 6164 (2011).
22. F. Rose, J. K. Bosworth, E. A. Dobisz, R. Ruiz, *Nanotechnology* **22**, 035603 (2011).
23. E. Kim *et al.*, *Soft Matter* **4**, 475 (2008).
24. Y. Wu *et al.*, *Nat. Mater.* **3**, 816 (2004).
25. K. Shin *et al.*, *Science* **306**, 76 (2004).
26. C. S. Henkee, E. L. Thomas, L. J. Fetters, *J. Mater. Sci.* **23**, 1685 (1988).
27. B. Yu, B. Li, Q. Jin, D. Ding, A. C. Shi, *Soft Matter* **7**, 10227 (2011).
28. R. Ruiz, E. Dobisz, T. R. Albrecht, *ACS Nano* **5**, 79 (2011).
29. W. A. Phillip, M. A. Hillmyer, E. L. Cussler, *Macromolecules* **43**, 7763 (2010).
30. See supplementary materials on *Science* Online.
31. J. K. W. Yang *et al.*, *Nat. Nanotechnol.* **5**, 256 (2010).
32. M. P. Stoykovich *et al.*, *Science* **308**, 1442 (2005).
33. M. P. Stoykovich *et al.*, *ACS Nano* **1**, 168 (2007).
34. Q. Peng, Y.-C. Tseng, S. B. Darling, J. W. Elam, *ACS Nano* **5**, 6 (2011).

Acknowledgments: Supported by a fellowship from NGS Singapore (A.T.K.G.), the Semiconductor Research Corporation, the Center on Functional Engineered and Nano Architectonics, Nanoelectronics Research Initiative, Singapore-MIT Alliance, Tokyo Electron, and Taiwan Semiconductor Manufacturing Company. We thank M. Mondol and J. Daley for technical assistance. A.T.K.G. would like to express his profound gratitude to T. C. Chong and S. N. Piramanayagam for their support. The Research Laboratory of Electronics Scanning-Electron-Beam Lithography Facility at MIT provided facilities for this work. A patent titled "Removable Templates for Directed Self-Assembly" has been filed with MIT.

Supplementary Materials

www.sciencemag.org/cgi/content/full/336/6086/1294/DC1
Materials and Methods
Figs. S1 to S18
References (*35–38*)

27 December 2011; accepted 20 April 2012
10.1126/science.1218437

Titanium and Zinc Oxide Nanoparticles Are Proton-Coupled Electron Transfer Agents

Joel N. Schrauben, Rebecca Hayoun, Carolyn N. Valdez, Miles Braten, Lila Fridley, James M. Mayer*

Oxidation/reduction reactions at metal oxide surfaces are important to emerging solar energy conversion processes, photocatalysis, and geochemical transformations. Here we show that the usual description of these reactions as electron transfers is incomplete. Reduced TiO_2 and ZnO nanoparticles in solution can transfer an electron and a proton to phenoxyl and nitroxyl radicals, indicating that e^- and H^+ are coupled in this interfacial reaction. These proton-coupled electron transfer (PCET) reactions are rapid and quantitative. The identification of metal oxide surfaces as PCET reagents has implications for the understanding and development of chemical energy technologies, which will rely on e^-/H^+ coupling.

Oxidation/reduction reactions of metal oxide materials (MO_x) play a key role in emerging energy technologies, as well as other processes such as photocatalytic wastewater remediation and self-cleaning surfaces (*1*) and geochemical redox formation and dissolution of minerals (*2*). These interfacial (solid/solution) redox processes are generally described just in terms of electron transfer (ET). For instance, the extensive literature on photochemical and electrochemical water splitting by MO_x is focused on the ET between surface-bound species and the valence and conduction bands of the solid. In dye-sensitized solar cells (DSSCs), the excited state of a dye injects an e^- into nanocrystalline TiO_2 (*3*). All of these disparate processes are affected by proton activity (the pH of aqueous interfaces), indicating a role for H^+. Here, we report well-characterized examples of reduced TiO_2 and ZnO nanoparticles (TiO_2/e^- and ZnO/e^-) reacting by proton-coupled electron transfer [PCET (*4*)]. TiO_2 and ZnO have been extensively studied from both fundamental and technological

Department of Chemistry, University of Washington, Seattle WA 98195, USA.

*To whom correspondence should be addressed. E-mail: mayer@chem.washington.edu

Fig. 1. Pictures of as-prepared and reduced (**A**) ZnO and (**B**) amorphous TiO_2 nanoparticles in toluene. UV-visible spectra of solutions of (**C**) ZnO (20-μM particles, 3.9-nm diameter) and (**D**) amorphous TiO_2 (51 μM, 3 nm) during irradiation with a 200-W Hg/Xe lamp. $^tBu_3ArO^\bullet$ titrations of (**E**) ZnO/e^- (0.51 mM, 3.9 nm) after 30 min of irradiation and (**F**) TiO_2/e^- (51 μM, 3 nm) after 10 min of irradiation.